















# Weakened Magnetic Braking in the Exoplanet Host Star 51 Peg

TRAVIS S. METCALFE <sup>1</sup>, KLAUS G. STRASSMEIER <sup>2</sup>, ILYA V. ILYIN <sup>2</sup>, DEREK BUZASI <sup>3</sup>, OLEG KOCHUKHOV <sup>4</sup>,  
THOMAS R. AYRES <sup>5</sup>, SARBANI BASU <sup>6</sup>, ASHLEY CHONTOS <sup>7</sup>, ADAM J. FINLEY <sup>8</sup>, VICTOR SEE <sup>9</sup>,  
KEIVAN G. STASSUN <sup>10</sup>, JENNIFER L. VAN SADERS <sup>11</sup>, ALDO G. SEPULVEDA <sup>11,\*</sup> AND GEORGE R. RICKER <sup>12</sup>

<sup>1</sup>White Dwarf Research Corporation, 9020 Brumm Trail, Golden, CO 80403, USA

<sup>2</sup>Leibniz-Institut für Astrophysik Potsdam (AIP), An der Sternwarte 16, D-14482 Potsdam, Germany

<sup>3</sup>Department of Chemistry and Physics, Florida Gulf Coast University, 10501 FGCU Blvd S, Fort Myers, FL 33965, USA

<sup>4</sup>Department of Physics and Astronomy, Uppsala University, Box 516, SE-75120 Uppsala, Sweden

<sup>5</sup>Center for Astrophysics and Space Astronomy, 389 UCB, University of Colorado, Boulder, CO 80309, USA

<sup>6</sup>Department of Astronomy, Yale University, PO Box 208101, New Haven, CT 06520-8101, USA

<sup>7</sup>Department of Astrophysical Sciences, Princeton University, Princeton, NJ 08544, USA

<sup>8</sup>Department of Astrophysics-AIM, University of Paris-Saclay and University of Paris, CEA, CNRS, Gif-sur-Yvette Cedex F-91191, France

<sup>9</sup>European Space Agency (ESA), European Space Research and Technology Centre (ESTEC), Keplerlaan 1, 2201 AZ Noordwijk, the Netherlands

<sup>10</sup>Vanderbilt University, Department of Physics & Astronomy, 6301 Stevenson Center Lane, Nashville, TN 37235, USA

<sup>11</sup>Institute for Astronomy, University of Hawai‘i, 2680 Woodlawn Drive, Honolulu, HI 96822, USA

<sup>12</sup>Department of Physics and Kavli Institute for Astrophysics and Space Science, Massachusetts Institute of Technology, Cambridge, MA 02139, USA

## ABSTRACT

The consistently low activity level of the old solar analog 51 Peg not only facilitated the discovery of the first hot Jupiter, but also led to the suggestion that the star could be experiencing a magnetic grand minimum. However, the 50 year time series showing minimal chromospheric variability could also be associated with the onset of weakened magnetic braking (WMB), where sufficiently slow rotation disrupts cycling activity and the production of large-scale magnetic fields by the stellar dynamo, thereby shrinking the Alfvén radius and inhibiting the efficient loss of angular momentum to magnetized stellar winds. In this Letter, we evaluate the magnetic evolutionary state of 51 Peg by estimating its wind braking torque. We use new spectropolarimetric measurements from the Large Binocular Telescope to reconstruct the large-scale magnetic morphology, we reanalyze archival X-ray measurements to estimate the mass-loss rate, and we detect solar-like oscillations in photometry from the Transiting Exoplanet Survey Satellite, yielding precise stellar properties from asteroseismology. Our estimate of the wind braking torque for 51 Peg clearly places it in the WMB regime, driven by changes in the mass-loss rate and the magnetic field strength and morphology that substantially exceed theoretical expectations. Although our revised stellar properties have minimal consequences for the characterization of the exoplanet, they have interesting implications for the current space weather environment of the system.

## 1. INTRODUCTION

Decades before the first hot Jupiter was discovered orbiting the old solar analog 51 Peg (Mayor & Queloz 1995), long-term monitoring of its chromospheric activity began at the Mount Wilson Observatory (MWO; Wilson 1968). These observations revealed nearly constant activity ( $\log R'_{\text{HK}} = -5.068$ ; Henry et al. 2000), below the solar minimum level ( $\log R'_{\text{HK}} = -4.984$ ; Egeland et al. 2017), starting in 1966 and continuing to the present day (Baliunas et al. 1995; Radick et al. 2018; Baum et al. 2022). Despite the low level of chromospheric activity, several seasons of the MWO data showed variability attributed to stellar rotation, with periods

ranging from 21.3–22.6 days (Henry et al. 2000). A reanalysis of these same measurements confirmed a rotation period  $P_{\text{rot}} = 21.9 \pm 0.4$  days from the observations in 1998 (Simpson et al. 2010), and highlighted a disagreement between the observed rotation period and the value predicted from the mean activity level (29 days; Wright et al. 2004).

The consistently low activity level, also seen in X-ray measurements, led to the suggestion of 51 Peg as a candidate Maunder minimum star (Poppenhäger et al. 2009). The Maunder minimum was the 70 year interval between 1645 and 1715 when very few sunspots appeared on the solar disk, and the phenomenon is more generally known as a magnetic grand minimum (Usoskin et al. 2007). The absence of long-term chromospheric variations in a 50 year time series cannot determine whether a star has temporarily or permanently lost

\* NSF Graduate Research Fellow

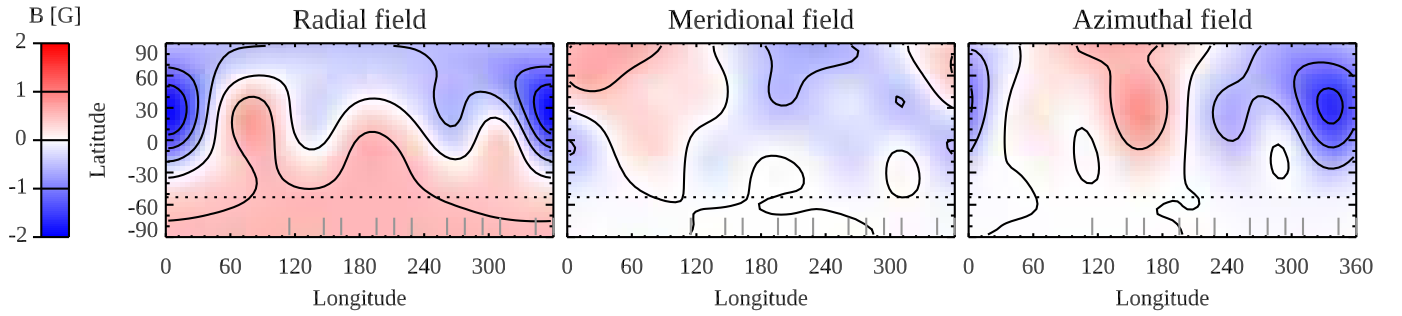


**Figure 1.** ZDI maps of the radial, meridional, and azimuthal field components of 51 Peg. Contours are shown with a step of 0.5 G. The dotted line corresponds to the lowest visible latitude. The vertical bars at the bottom of each panel show the central longitude of each LBT observation.

its activity cycle. The only unambiguous evidence that a star has experienced a magnetic grand minimum is the observation of a transition from cycling to non-cycling or from non-cycling to cycling. Currently, such evidence only exists for one star, HD 166620 (Baum et al. 2022; Luhn et al. 2022). Another interpretation of constant activity stars like 51 Peg was put forward by Metcalfe & van Saders (2017), who suggested that they may represent the disappearance of activity cycles associated with the onset of weakened magnetic braking (WMB; van Saders et al. 2016, 2019; Hall et al. 2021). In this scenario, sufficiently slow rotation disrupts cycling activity and the production of large-scale magnetic fields by the stellar dynamo, thereby shrinking the Alfvén radius and inhibiting the efficient loss of angular momentum to magnetized stellar winds (Metcalfe et al. 2022).

In this Letter, we evaluate the magnetic evolutionary state of 51 Peg by estimating its wind braking torque using the prescription of Finley & Matt (2018). In Section 2.1 we use new spectropolarimetric measurements from the  $2\times 8.4$  m Large Binocular Telescope (LBT) to reconstruct the large-scale magnetic morphology of 51 Peg. In Section 2.2 we use archival X-ray measurements to estimate the mass-loss rate from the empirical relation of Wood et al. (2021). In Section 2.3 we use a detection of solar-like oscillations from the Transiting Exoplanet Survey Satellite (TESS; Ricker et al. 2014) to place constraints on the stellar radius, mass, and age. In Section 3 we bring the measurements together to estimate the wind braking torque for 51 Peg, and in Section 4 we discuss the implications of WMB on the space weather environment of this iconic planetary system.

## 2. STELLAR PROPERTIES

### 2.1. Spectropolarimetry

We observed 51 Peg from the LBT on 12 nights between 2022 November 18 and 2022 December 3 using the Potsdam Echelle Polarimetric and Spectroscopic Instrument (PEPSI; Strassmeier et al. 2015, 2018). The instrument configuration and data reduction methods were the same as those described in Metcalfe et al. (2019), and we derived precise mean intensity and circular polarization (Stokes  $V$ ) pro-

files at each epoch using the least-squares deconvolution (LSD; Kochukhov et al. 2010) technique. We did not consider linear polarization (Stokes  $Q$  and  $U$ ) because the Zeeman signatures are typically an order of magnitude smaller (Kochukhov et al. 2011). The LSD analysis employed spectral line data from the VALD database (Ryabchikova et al. 2015), and we adopted spectroscopic parameters from Brewer et al. (2016). The observations spanned 15 nights, corresponding to central longitudes covering 68% of the 21.9 day rotation period, allowing us to reconstruct the large-scale magnetic field with Zeeman Doppler Imaging (ZDI; Kochukhov 2016). Although poor weather prevented additional observations that could have provided redundant information for the inversion procedure, our set of disk-integrated Stokes  $V$  profiles provide some constraints at all stellar longitudes. A complete archive of the reduced data is available at [doi:10.5281/zenodo.8381444](https://doi.org/10.5281/zenodo.8381444).

The inclination of the stellar rotation axis was estimated using the analytic expressions from Bowler et al. (2023) that approximate the Bayesian framework of Masuda & Winn (2020) to calculate stellar inclination posteriors given measurements of  $v\sin i$ , rotation period, and radius. The posterior inclination distribution for 51 Peg (from the spectroscopic  $v\sin i$ , the chromospheric rotation period, and the asteroseismic radius in Section 2.3) peaks at  $i = 53^\circ$ , with a 68% credible interval between  $42^\circ$  and  $78^\circ$ . The lower bound corresponds to  $v\sin i = 1.8 \text{ km s}^{-1}$  determined by Morris et al. (2019), while the upper bound is comparable to the orbital inclination of 51 Peg b inferred by Birkby et al. (2017). Lower inclinations yield less geometric cancellation, and thus weaker inferred fields for a given set of Stokes  $V$  profiles. Higher inclinations are disfavored by the absence of transits in the 51 Peg system. We adopt the most probable value of the inclination for our fiducial model, and assess the impact of the uncertainty in Section 3.

Results of the ZDI inversion for 51 Peg are presented in Figure 1, which shows Mercator maps of the radial, meridional, and azimuthal components of the large-scale magnetic field. The vertical bars at the bottom of each panel show the central longitude of each LBT observation, and regions of

the ZDI map below the dotted lines in Figure 1 are not visible from Earth. The magnetic morphology is predominantly poloidal (86% of the field energy is in poloidal components) and nonaxisymmetric ( $m \neq 0$  harmonic modes contain 74% of the field energy). The average field strength is  $\langle B \rangle = 0.68$  G with a maximum local strength of 2.28 G. The field structure is dominated by a nonaxisymmetric dipole (strength 0.77 G, obliquity  $143^\circ$  towards the positive pole), which comprises 64% of the field energy. The sum of the quadrupole and octupole modes contribute 31% of the field energy. The fit to the observed Stokes  $V$  profiles is shown in Figure 2.

The rate of angular momentum loss due to the magnetized stellar wind depends primarily on the radial component of the large-scale field. The prescription of [Finley & Matt \(2018\)](#) that we use in Section 3 to estimate the wind braking torque requires polar field strengths of the axisymmetric ( $m = 0$ ) dipole, quadrupole, and octupole components of this field. The observed ZDI map is dominated by nonaxisymmetric ( $m \neq 0$ ) components, but we follow the procedure described in [Metcalf et al. \(2022\)](#) to calculate the equivalent polar field strengths ( $B_d, B_q, B_o$ ) for use with the wind braking prescription. For each spherical harmonic degree  $\ell$ , this procedure calculates the total magnetic flux  $\Phi_\ell = \int |B_\ell \cdot dA|$ , where the integral is over the stellar surface. The equivalent polar field strength comes from the axisymmetric configuration for a given spherical harmonic degree that yields the same total magnetic flux as that calculated from both the axisymmetric and nonaxisymmetric components of the ZDI map. There is a simple analytical relation between the equivalent polar field strength and the magnetic flux from ZDI for each spherical harmonic degree:

$$B_d = \frac{1}{2\pi R_\star^2} \Phi_d, \quad B_q = \frac{3\sqrt{3}}{8\pi R_\star^2} \Phi_q, \quad B_o = \frac{10}{13\pi R_\star^2} \Phi_o \quad (1)$$

where  $R_\star$  is the stellar radius and  $\Phi_{d,q,o}$  is the magnetic flux integrated over the surface for the dipole, quadrupole, and octupole components of the ZDI map, respectively. The values of  $B_d, B_q, B_o$  from our ZDI map are listed in Table 1.

## 2.2. X-Ray Data

[Poppenhäger et al. \(2009\)](#) described previous X-ray observations of 51 Peg from ROSAT, XMM-Newton, and Chandra. The ROSAT observation was carried out in late-1992, with a 12 ks effective exposure by the PSPC instrument. Sixteen years later in mid-2008, XMM-Newton obtained a deep 55 ks pointing on 51 Peg. Six months after that, Chandra obtained two short 4.9 ks exposures on the same day with the HRC-I and ACIS-S instruments. [Poppenhäger et al.](#) carried out a detailed analysis of these observations, but they adopted a single-temperature plasma model to calculate the crucial energy conversion factors that translate count rates into physical fluxes. They obtained a large range of X-ray

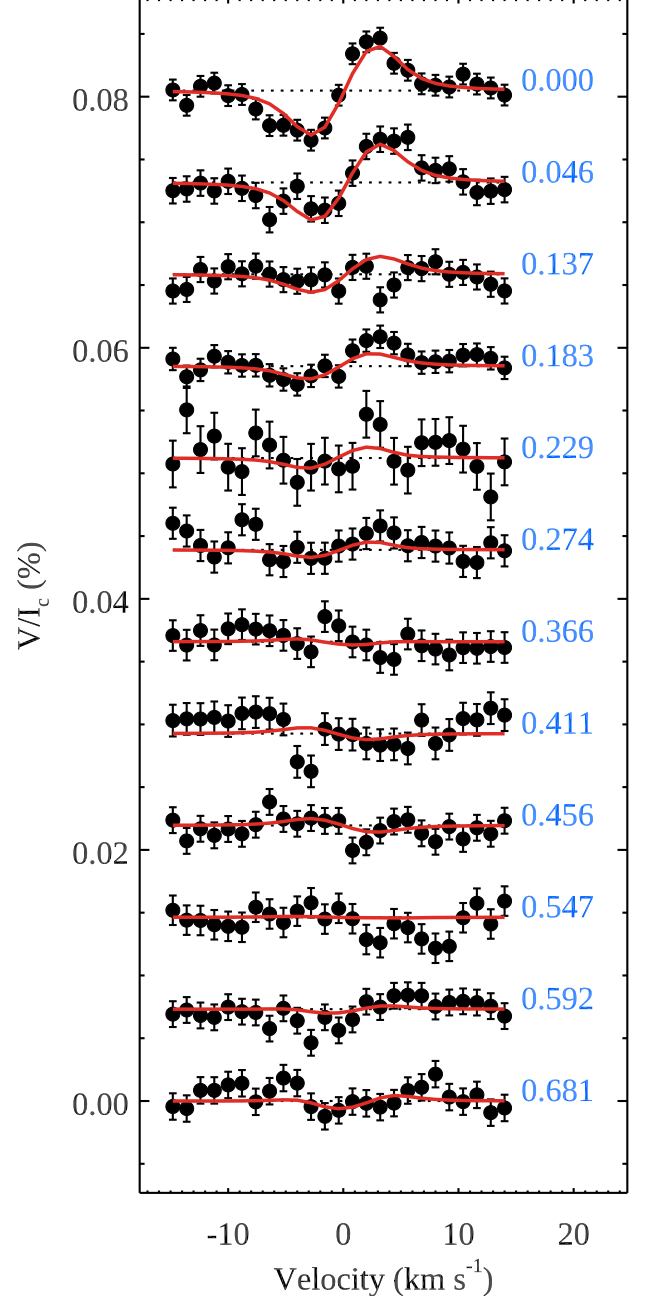


**Figure 2.** ZDI fit to the observed Stokes  $V$  LSD profiles for 51 Peg. Observations (points) and model profiles (solid lines) are shifted vertically according to the rotational phase, which is indicated on the right of each profile.

luminosities for 51 Peg,  $\log L_X = 26.1\text{--}27.2$  erg s $^{-1}$ , with the lower and upper limits corresponding to the XMM/MOS1+2 and Chandra/HRC-I measurements, respectively.

We carried out an independent assessment of the archival X-ray data, using a new modeling approach that circumvents the issue of choosing an appropriate single coronal temperature ([Ayres & Buzasi 2022](#)). We reached similar conclusions to [Poppenhäger et al. \(2009\)](#) for the ROSAT and

**Table 1.** Properties of the Exoplanet Host Star 51 Peg

	51 Peg	Source
$T_{\text{eff}}$ (K)	$5758 \pm 78$	1
[M/H] (dex)	$+0.18 \pm 0.07$	1
$\log g$ (dex)	$4.32 \pm 0.08$	1
$v \sin i$ (km s $^{-1}$ )	$2.0 \pm 0.5$	1
$B - V$ (mag)	0.67	2
$\log R'_{\text{HK}}$ (dex)	$-5.068$	2
$P_{\text{rot}}$ (days)	$21.9 \pm 0.4$	3
$ B_d $ (G)	0.770	4
$ B_q $ (G)	0.441	4
$ B_o $ (G)	0.652	4
$\log L_X$ (erg s $^{-1}$ )	$26.8 \pm 0.2$	5
Mass-loss rate ( $\dot{M}_{\odot}$ )	$0.38 \pm 0.13$	5
$\Delta\nu$ ( $\mu\text{Hz}$ )	$114.6 \pm 1.2$	6
$\nu_{\text{max}}$ ( $\mu\text{Hz}$ )	$2474 \pm 123$	6
Luminosity ( $L_{\odot}$ )	$1.398 \pm 0.016$	6
Radius ( $R_{\odot}$ )	$1.152 \pm 0.009$	6
Mass ( $M_{\odot}$ )	$1.09 \pm 0.02$	6
Age (Gyr)	$4.8^{+0.7}_{-0.4}$	6
Torque ( $10^{30}$ erg)	$0.224^{+0.039}_{-0.075}$	7

**References**—(1) [Brewer et al. \(2016\)](#); (2) [Henry et al. \(2000\)](#); (3) [Simpson et al. \(2010\)](#); (4) Section 2.1; (5) Section 2.2; (6) Section 2.3; (7) Section 3

Chandra observations. However, as noted by those authors, the deep XMM-Newton pointing on 51 Peg yielded surprisingly minimal detections—probably owing to the use of the thick optical blocking filter, which significantly degrades the soft response of the camera system. The large energy conversion factors for the XMM pn and MOS modules under these circumstances render any derived fluxes problematic. From the ROSAT and Chandra data alone, we obtained a range of X-ray luminosities  $\log L_X = 26.6\text{--}27.0$  erg s $^{-1}$  in the 0.1–2.4 keV band. Considering the minimal chromospheric variability of 51 Peg ([Baum et al. 2022](#)), the dispersion in our X-ray luminosity estimates probably arises from uncertainties in the instrumental calibrations at the soft energies that are characteristic of low-activity coronal sources. The importance of this calibration issue is evidenced by the fact that the Chandra HRC-I and ACIS-S pointings within less than 2 h of each other yield X-ray flux estimates that differ by 60%.

Using the empirical relation  $\dot{M} \propto F_X^{0.77}$  from [Wood et al. \(2021\)](#), we can estimate the mass-loss rate for 51 Peg from the range of X-ray luminosities determined above and the asteroseismic radius in Section 2.3. The lower bound on the X-ray luminosity yields  $\dot{M} = 0.25 \dot{M}_{\odot}$  while the upper bound yields  $\dot{M} = 0.51 \dot{M}_{\odot}$ . For the estimates of wind braking torque in Section 3, we adopt the average of these two

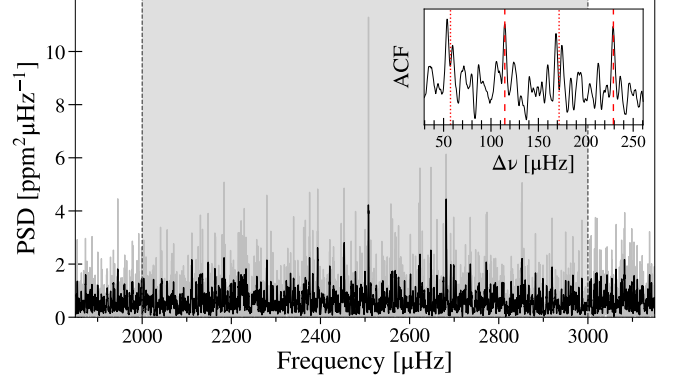


**Figure 3.** Power spectrum of 51 Peg centered on the power excess due to solar-like oscillations. The shaded region is used to calculate an autocorrelation, shown in the inset. Dashed lines in the inset represent expected peaks in the ACF due to the characteristic spacings of p-modes.

values with an uncertainty that reflects the full range of possible X-ray luminosities (see Table 1).

### 2.3. Asteroseismology

The TESS mission observed 51 Peg at 20 s cadence during Sector 56 (2022 September 1–30). Following the procedures described in [Metcalf et al. \(2023a\)](#), we extracted a custom light curve from the TESS target pixel files, substantially improving the signal to noise ratio (S/N) compared to the data product from the Science Processing Operations Center. Briefly, this procedure starts with a light curve from the pixel with the most signal, and includes additional pixels one at a time until the S/N no longer improves. The resulting light curve was detrended against centroid pixel coordinates and high-pass filtered with a cutoff frequency of 100  $\mu\text{Hz}$  to remove any residual instrumental signatures.

Figure 3 shows the power spectrum of 51 Peg computed from the TESS photometry, centered on the power excess near 2500  $\mu\text{Hz}$ . To confirm that the observed power excess is due to solar-like oscillations we used `pySYD` ([Chontos et al. 2022; Huber et al. 2009](#)), which implements an autocorrelation technique to identify and characterize the global oscillation parameters ( $\Delta\nu$ ,  $\nu_{\text{max}}$ ). The autocorrelation function (ACF) in the inset of Figure 3 is calculated from the shaded region of the power spectrum, showing strong peaks at the expected spacings ( $\Delta\nu = 114.6 \pm 1.2 \mu\text{Hz}$ ) and confirming an asteroseismic detection with  $\nu_{\text{max}} = 2474 \pm 123 \mu\text{Hz}$ .

In addition to the global oscillation parameters, we adopted observational constraints on the effective temperature  $T_{\text{eff}}$  and metallicity [M/H] from [Brewer et al. \(2016\)](#), as well as a bolometric luminosity  $L$  derived from the spectral energy distribution following the procedures described in [Stassun et al. \(2017, 2018\)](#). These constraints provided the inputs for grid-based modeling with the Yale-Birmingham pipeline ([Basu et al. 2010, 2012; Gai et al. 2011](#)), using the same grid of



models constructed with YREC (Demarque et al. 2008) and following the same procedures described in Metcalfe et al. (2021). The resulting determinations of the asteroseismic radius, mass, and age of 51 Peg are listed in Table 1.

### 3. WIND BRAKING TORQUE

We now have all of the required inputs to estimate the wind braking torque for 51 Peg, following the prescription of Finley & Matt (2018)<sup>1</sup>. Bringing together the equivalent polar field strengths from our ZDI map in Section 2.1, the mass-loss rate from the empirical relation of Wood et al. (2021) in Section 2.2, the chromospheric rotation period from Simpson et al. (2010), and the asteroseismic mass and radius from Section 2.3, we calculate a wind braking torque of  $0.224^{+0.039}_{-0.075} \times 10^{30}$  erg. The uncertainty includes a contribution from the inclination, evaluated at the extremes of the 68% credible interval between  $42^\circ$  and  $78^\circ$ . For each inclination, we inverted a new ZDI map from the observations, calculated the equivalent polar field strengths for each spherical harmonic degree, and updated our estimate of the wind braking torque. With the other parameters fixed, the resulting torque at both extremes of the inclination was slightly lower than for our fiducial model ( $0.196$  and  $0.214 \times 10^{30}$  erg at  $42^\circ$  and  $78^\circ$ , respectively), bolstering our conclusions.

In Figure 4, we compare 51 Peg with similarly estimated wind braking torques for two slightly hotter stars (Metcalfe et al. 2021), four solar analogs (Metcalfe et al. 2022), and two cooler G-type stars (Metcalfe et al. 2023b). Rossby numbers were calculated from the Gaia  $G_{BP} - G_{RP}$  color using the asteroseismic calibration of Corsaro et al. (2021), normalized to the solar value on this scale ( $Ro_\odot = 0.496$ ). The wind braking torque has been normalized to the value for HD 76151 ( $4.17 \times 10^{30}$  erg) to facilitate a comparison with theoretical models. Horizontal error bars come from the uncertainty in the rotation period, while vertical error bars reflect the range of possible torques when all input quantities are shifted by  $\pm 1\sigma$ . The gray shaded area represents our empirical constraint on the critical Rossby number for the onset of WMB ( $Ro_{\text{crit}}/Ro_\odot = 0.92 \pm 0.01$ ), and the dotted yellow line shows the evolution of the torque for HD 76151 ( $M = 1.05 M_\odot$ ) from a standard spin-down model (van Saders & Pinsonneault 2013). The mass-dependence of stellar spin-down can shift this standard model up or down by a factor of two for the mass range shown in Figure 4.

The wind braking torque for 51 Peg clearly places it in the WMB regime, with the ZDI map providing a much stronger constraint than  $\rho$  CrB or the components of 16 Cyg, which rely on upper limits from statistical non-detections of the large-scale magnetic field. We compare the fiducial models of 51 Peg and HD 76151 (see Metcalfe et al. 2022) to eval-

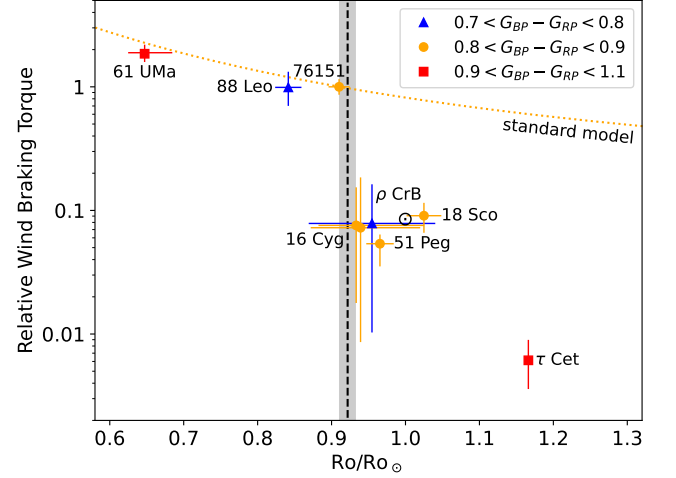


**Figure 4.** Estimated wind braking torque relative to HD 76151 as a function of Rossby number normalized to the solar value. Points are grouped by Gaia color, corresponding to solar analogs (yellow circles) and hotter (blue triangles) or cooler (red squares) stars. The gray shaded area represents our empirical constraint on the critical Rossby number for the onset of WMB ( $Ro_{\text{crit}}/Ro_\odot = 0.92 \pm 0.01$ ).

uate the relative importance of various contributions to the total decrease in torque. The wind braking torque decreases by nearly a factor of 20 ( $-95\%$ ) between the ages of these two stars (2.6–4.8 Gyr), dominated by changes in the mass-loss rate ( $-81\%$ ) and magnetic field strength and morphology ( $-78\%$ ) with smaller contributions from the differences in rotation period ( $-6\%$ ) and stellar mass ( $-0.9\%$ ). These decreases are substantially offset by evolutionary changes in the stellar radius ( $+75\%$ ). The overall decrease in the wind braking torque is larger for 51 Peg (by 4.8 Gyr) than from a similar comparison of 18 Sco (at 3.7 Gyr) and HD 76151 in Metcalfe et al. (2022), but it reinforces the relatively equal importance of changes in the mass-loss rate and magnetic field strength and morphology ( $-69\%$  and  $-65\%$ , respectively for 18 Sco) near the onset of WMB.

A comparison of the fiducial models for 51 Peg and 18 Sco suggests that the wind braking torque continues to decrease ( $-41\%$ ) at later evolutionary phases (3.7–4.8 Gyr). As with the components of 16 Cyg (see Metcalfe et al. 2022), the subsequent decrease in wind braking torque becomes dominated by the evolution of magnetic field strength and morphology ( $-40\%$ ) with smaller contributions from differences in the mass-loss rate ( $-36\%$ ) and stellar mass ( $-2\%$ ), offset by evolutionary changes in stellar radius ( $+51\%$ ) and the difference in rotation period ( $+4\%$ ). Although changes in the magnetic field strength and morphology continue to favor a lower wind braking torque ( $-33\%$ ) between the ages of 51 Peg and 16 Cyg A (4.8–7.0 Gyr), this decrease is overwhelmed by the evolution of mass-loss rate ( $+61\%$ ) and stellar radius ( $+21\%$ ), with small contributions from differences in rotation period ( $+7\%$ ) and stellar mass ( $+0.4\%$ ).

<sup>1</sup> <https://github.com/travismetcalfe/FinleyMatt2018>

Standard spin-down models fail to predict the substantial changes in wind braking torque that are suggested by the observations. While these models generally reproduce the evolution prior to the onset of WMB (dotted line in Figure 4), they predict a decrease of only  $-12\%$  in the wind braking torque between HD 76151 and 51 Peg, rather than the  $-95\%$  estimated above. This failure can be traced to underestimated changes in both the mass-loss rate (or  $L_X$ ) and the magnetic field strength, as well as neglected changes in magnetic morphology. Standard models scale the mass-loss rate as  $\dot{M} \sim L/\text{Ro}^2$  and the magnetic field strength as  $B \sim P_{\text{phot}}^{1/2}/\text{Ro}$ , where  $P_{\text{phot}}$  is the photospheric pressure (van Saders & Pinsonneault 2013). According to these models, the mass-loss rate is predicted to decrease by  $-9\%$  and the magnetic field strength by  $-6\%$  between HD 76151 and 51 Peg, while the observations suggest a decrease of  $-95\%$  in the mass-loss rate and  $-57\%$  in the magnetic field strength (from the difference in the activity proxy  $\log R'_{\text{HK}}$ ). The average strength of the large-scale field from spectropolarimetry decreases by  $-78\%$  (See et al. 2019), suggesting that changes in magnetic morphology are also important.

#### 4. DISCUSSION

Using new observational constraints from LBT spectropolarimetry and TESS asteroseismology, we have demonstrated that the wind braking torque of the exoplanet host star 51 Peg places it firmly in the WMB regime. This provides a natural explanation for the disagreement between the observed rotation period (21.9 days) and that predicted from its mean activity level (29 days; Wright et al. 2004). At the onset of WMB, rotation and activity decouple (Metcalf et al. 2016; Metcalfe & Egeland 2019) as the magnetic fields that had previously facilitated the efficient loss of angular momentum to stellar winds grow weaker and cascade to smaller spatial scales. Beyond this transition, the rotation period only changes with the stellar moment of inertia (van Saders et al. 2016) while the activity level continues to decline with age (Lorenzo-Oliveira et al. 2018; Huber et al. 2022) as mechanical energy from convection becomes the dominant source of chromospheric heating (Böhm-Vitense 2007). Our asteroseismic age for 51 Peg is older than expected from its rotation period ( $2.9 \pm 0.5$  Gyr; Barnes 2007), but younger than expected from its activity level (7 Gyr; Donahue 1998), so other factors such as non-solar metallicity may also contribute to the erroneous prediction of rotation period from activity level (see Saar & Testa 2012). It is now clear that WMB begins before stars reach  $\text{Ro}_{\odot}$ , and our empirical constraint on the value of  $\text{Ro}_{\text{crit}}/\text{Ro}_{\odot}$  is consistent with that derived from the analysis of a larger sample of stars with asteroseismic rotation periods and ages (Saunders et al. 2023).

Our revised stellar properties and estimated wind braking torque for 51 Peg have minimal consequences for the characterization of the exoplanet, but interesting implications for the current space weather environment of the system. The most recent orbital solution for 51 Peg b (Rosenthal et al. 2021) adopted a stellar mass that was only 2% lower than the asteroseismic mass determined in Section 2.3. The resulting update to the planetary mass would be well within the quoted uncertainties. Considering our characterization of the large-scale field and mass-loss rate of 51 Peg, direct magnetic interactions between the star and planet are unlikely. The Alfvén radius of our fiducial wind model for 51 Peg is  $R_A = 4.7 R_*$ , while the semi-major axis of 51 Peg b is much larger at  $a = 9.8 R_*$ . Even prior to the onset of WMB, assuming the magnetic field properties and mass-loss rate of HD 76151 (Metcalf et al. 2022), the Alfvén radius of 51 Peg would have been  $R_A = 5.5 R_*$ , still well inside the planetary orbit. Nevertheless, standard spin-down models predict that without WMB, 51 Peg would have had both a higher mass-loss rate and a stronger magnetic field with more large-scale open field where energetic eruptions could escape (Garraffo et al. 2015), creating a harsher space weather environment than actually exists. Consequently, older stars beyond the onset of WMB may provide a more stable environment for the development of technological civilizations.

T.S.M. is supported by NASA grant 80NSSC22K0475 and NSF grant AST-2205919. D.B. gratefully acknowledges support from NASA (NNX16AB76G, 80NSSC22K0622) and the Whitaker Endowed Fund at Florida Gulf Coast University. O.K. acknowledges support by the Swedish Research Council (grant agreement no. 2019-03548), the Swedish National Space Agency, and the Royal Swedish Academy of Sciences. S.B. is supported by NSF grant AST-2205026. V.S. acknowledges support from the European Space Agency (ESA) as an ESA Research Fellow. A.G.S. acknowledges support from the National Science Foundation Graduate Research Fellowship Program under Grant No. 1842402. The LBT is an international collaboration among institutions in the United States, Italy and Germany. This paper includes data collected with the TESS mission, obtained from the Mikulski Archive for Space Telescopes at the Space Telescope Science Institute (STScI). The specific observations analyzed can be accessed via [doi:10.17909/emgj-gq45](https://doi.org/10.17909/emgj-gq45). Funding for the TESS mission is provided by the NASA Explorer Program. STScI is operated by the Association of Universities for Research in Astronomy, Inc., under NASA contract NAS 5-26555. This research was supported in part by the Nonprofit Adopt a Star program ([adoptastar.org](https://adoptastar.org)) administered by White Dwarf Research Corporation.

## REFERENCES

- Ayres, T., & Buzasi, D. 2022, *ApJS*, 263, 41
- Baliunas, S. L., et al. 1995, *ApJ*, 438, 269
- Barnes, S. A. 2007, *ApJ*, 669, 1167
- Basu, S., Chaplin, W. J., & Elsworth, Y. 2010, *ApJ*, 710, 1596
- Basu, S., Verner, G. A., Chaplin, W. J., & Elsworth, Y. 2012, *ApJ*, 746, 76
- Baum, A. C., Wright, J. T., Luhn, J. K., & Isaacson, H. 2022, *AJ*, 163, 183
- Birkby, J. L., de Kok, R. J., Brogi, M., Schwarz, H., & Snellen, I. A. G. 2017, *AJ*, 153, 138
- Böhm-Vitense, E. 2007, *ApJ*, 657, 486
- Bowler, B. P., et al. 2023, *AJ*, 165, 164
- Brewer, J. M., Fischer, D. A., Valenti, J. A., & Piskunov, N. 2016, *ApJS*, 225, 32
- Chontos, A., Huber, D., Sayeed, M., & Yamsiri, P. 2022, *The Journal of Open Source Software*, 7, 3331
- Corsaro, E., Bonanno, A., Mathur, S., García, R. A., Santos, A. R. G., Breton, S. N., & Khalatyan, A. 2021, *A&A*, 652, L2
- Demarque, P., Guenther, D. B., Li, L. H., Mazumdar, A., & Straka, C. W. 2008, *Ap&SS*, 316, 31
- Donahue, R. A. 1998, in *Astronomical Society of the Pacific Conference Series*, Vol. 154, *Cool Stars, Stellar Systems, and the Sun*, ed. R. A. Donahue & J. A. Bookbinder, 1235
- Egeland, R., Soon, W., Baliunas, S., Hall, J. C., Pevtsov, A. A., & Bertello, L. 2017, *ApJ*, 835
- Finley, A. J., & Matt, S. P. 2018, *ApJ*, 854, 78
- Gai, N., Basu, S., Chaplin, W. J., & Elsworth, Y. 2011, *ApJ*, 730, 63
- Garraffo, C., Drake, J. J., & Cohen, O. 2015, *ApJ*, 813, 40
- Hall, O. J., et al. 2021, *Nature Astronomy*, 5, 707
- Henry, G. W., Baliunas, S. L., Donahue, R. A., Fekel, F. C., & Soon, W. 2000, *ApJ*, 531, 415
- Huber, D., Stello, D., Bedding, T. R., Chaplin, W. J., Arentoft, T., Quirion, P. O., & Kjeldsen, H. 2009, *Communications in Asteroseismology*, 160, 74
- Huber, D., et al. 2022, *AJ*, 163, 79
- Kochukhov, O. 2016, in *Lecture Notes in Physics*, Berlin Springer Verlag, ed. J.-P. Rozelot & C. Neiner, Vol. 914, 177
- Kochukhov, O., Makaganiuk, V., & Piskunov, N. 2010, *A&A*, 524, A5
- Kochukhov, O., et al. 2011, *ApJL*, 732, L19
- Lorenzo-Oliveira, D., et al. 2018, *A&A*, 619, A73
- Luhn, J. K., Wright, J. T., Henry, G. W., Saar, S. H., & Baum, A. C. 2022, *ApJL*, 936, L23
- Masuda, K., & Winn, J. N. 2020, *AJ*, 159, 81
- Mayor, M., & Queloz, D. 1995, *Nature*, 378, 355
- Metcalfe, T. S., & Egeland, R. 2019, *ApJ*, 871, 39
- Metcalfe, T. S., Egeland, R., & van Saders, J. 2016, *ApJL*, 826, L2
- Metcalfe, T. S., Kochukhov, O., Ilyin, I. V., Strassmeier, K. G., Godoy-Rivera, D., & Pinsonneault, M. H. 2019, *ApJL*, 887, L38
- Metcalfe, T. S., & van Saders, J. 2017, *SoPh*, 292, 126
- Metcalfe, T. S., et al. 2021, *ApJ*, 921, 122
- . 2022, *ApJL*, 933, L17
- . 2023a, *AJ*, 166, 167
- . 2023b, *ApJL*, 948, L6
- Morris, B. M., Curtis, J. L., Sakari, C., Hawley, S. L., & Agol, E. 2019, *AJ*, 158, 101
- Poppenhäger, K., Robrade, J., Schmitt, J. H. M. M., & Hall, J. C. 2009, *A&A*, 508, 1417
- Radick, R. R., Lockwood, G. W., Henry, G. W., Hall, J. C., & Pevtsov, A. A. 2018, *ApJ*, 855, 75
- Ricker, G. R., et al. 2014, in *Proceedings of the SPIE*, Vol. 9143, 914320
- Rosenthal, L. J., et al. 2021, *ApJS*, 255, 8
- Ryabchikova, T., Piskunov, N., Kurucz, R. L., Stempels, H. C., Heiter, U., Pakhomov, Y., & Barklem, P. S. 2015, *PhyS*, 90, 054005
- Saar, S. H., & Testa, P. 2012, in *Comparative Magnetic Minima: Characterizing Quiet Times in the Sun and Stars*, ed. C. H. Mandrini & D. F. Webb, Vol. 286, 335–345
- Saunders, N., et al. 2023, *ApJ*, submitted, (arXiv:2309.05666)
- See, V., et al. 2019, *ApJ*, 876, 118
- Simpson, E. K., Baliunas, S. L., Henry, G. W., & Watson, C. A. 2010, *MNRAS*, 408, 1666
- Stassun, K. G., Collins, K. A., & Gaudi, B. S. 2017, *AJ*, 153, 136
- Stassun, K. G., Corsaro, E., Pepper, J. A., & Gaudi, B. S. 2018, *AJ*, 155, 22
- Strassmeier, K. G., et al. 2015, *Astronomische Nachrichten*, 336, 324
- Strassmeier, K. G., et al. 2018, in *Ground-based and Airborne Instrumentation for Astronomy VII*, ed. C. J. Evans, L. Simard, & H. Takami, Vol. 10702, 1070212
- Usoskin, I. G., Solanki, S. K., & Kovaltsov, G. A. 2007, *A&A*, 471, 301
- van Saders, J. L., Ceillier, T., Metcalfe, T. S., Silva Aguirre, V., Pinsonneault, M. H., García, R. A., Mathur, S., & Davies, G. R. 2016, *Nature*, 529, 181
- van Saders, J. L., & Pinsonneault, M. H. 2013, *ApJ*, 776, 67
- van Saders, J. L., Pinsonneault, M. H., & Barbieri, M. 2019, *ApJ*, 872, 128
- Wilson, O. C. 1968, *ApJ*, 153, 221
- Wood, B. E., et al. 2021, *ApJ*, 915, 37
- Wright, J. T., Marcy, G. W., Butler, R. P., & Vogt, S. S. 2004, *ApJS*, 152, 261